Atmos. Chem. Phys. Discuss., 10, 15921–15962, 2010
www.atmos-chem-phys-discuss.net/10/15921/2010/
doi:10.5194/acpd-10-15921-2010

Atmospheric Chemistry and Physics Discussions

Southeast Pacific stratocumulus clouds, precipitation and boundary layer structure sampled along 20 S during VOCALS-REx

C. S. Bretherton[1], R. Wood[1], R. C. George[1], D. Leon[2], G. Allen[3], and X. Zheng[4]

[1]Department of Atmospheric Science, University of Washington, Seattle, Washington, USA
[2]Department of Atmospheric Science, University of Wyoming, Laramie, Wyoming, USA
[3]Centre for Atmospheric Sciences, University of Manchester, Manchester, UK
[4]Rosenstiel School of Marine and Atmospheric Sciences, University of Miami, Miami, Florida, USA

Received: 12 June 2010 – Accepted: 22 June 2010 – Published: 29 June 2010

Correspondence to: C. S. Bretherton (breth@washington.edu)

Published by Copernicus Publications on behalf of the European Geosciences Union.

Abstract

Multiplatform airborne, ship-based, and land-based observations from 16 October–15 November 2008 during the VOCALS Regional Experiment (REx) are used to document the typical structure of the Southeast Pacific stratocumulus-topped boundary layer and lower free troposphere on a transect along 20° S between the coast of Northern Chile and a buoy 1500 km offshore. Strong systematic gradients in clouds, precipitation and vertical structure are modulated by synoptically and diurnally-driven variability. The boundary layer is generally capped by a strong (10–12 K), sharp inversion. In the coastal zone, the boundary layer is typically 1 km deep, fairly well mixed, and topped by thin, nondrizzling stratocumulus with haccumulation-mode aerosol and cloud droplet concentrations exceeding 200 cm^{-3}. Far offshore, the boundary layer depth is typically deeper (1600 m) and more variable, and the vertical structure is usually decoupled. The offshore stratocumulus typically have strong mesoscale organization, much higher peak liquid water paths, extensive drizzle, and cloud droplet concentrations below 100 cm^{-3}, sometimes with embedded pockets of open cells with lower droplet concentrations. The lack of drizzle near the coast is not just a microphysical response to high droplet concentrations; smaller cloud depth and liquid water path than further offshore appear comparably important.

Moist boundary layer air is heated and mixed up along the Andean slopes, then advected out over the top of the boundary layer above adjacent coastal ocean regions. Well offshore, the lower free troposphere is typically much drier. This promotes strong cloud-top radiative cooling and stronger turbulence in the clouds offshore. In conjunction with a slightly cooler free troposphere, this may promote stronger entrainment that maintains the deeper boundary layer seen offshore.

Winds from ECMWF and NCEP operational analyses have an rms difference of only 1 $m\,s^{-1}$ from collocated airborne leg-mean observations in the boundary layer and 2 $m\,s^{-1}$ above the boundary layer. This supports the use of trajectory analysis for interpreting REx observations. Two-day back-trajectories from the 20° S transect suggest

ACPD

10, 15921–15962, 2010

VOCALS-REx 20 S boundary layer, clouds and precipitation

C. S. Bretherton et al.

that eastward of 75° W, boundary layer (and often free-tropospheric) air has usually been exposed to Chilean coastal aerosol sources, while at 85° W, neither boundary-layer or free-tropospheric air has typically had such contact.

1 Introduction

The cool waters of the Southeast Pacific are blanketed by the world's largest and most persistent subtropical stratocumulus regime, often extending 2000 km or more off the west coasts of Northern Chile, Peru and Ecuador. The clouds show strong and persistent microphysical contrasts with much larger droplet effective radii further offshore in regions far from local pollution sources. In these offshore regions, drizzle organized into mesoscale cells is common. These characteristics make this an ideal region to gather a dataset that comprehensively test global model prediction of the interaction of stratocumulus cloud topped boundary layers, aerosol/chemical and precipitation processes.

This thinking motivated the VAMOS Ocean-Cloud-Atmosphere-Land Study Regional Experiment (VOCALS-REx) in October-November 2008. A primary goal of REx was to gather a comprehensive multiplatform dataset along 20° S from the Chilean coast (70° W) out to a climate reference buoy at 85° W for model evaluation, focusing on the lowest 3 km of the atmosphere. Multiple aircraft missions using a consistent flight plan complemented ship and land-based measurements during a month of intensive sampling.

The focus of this paper is the mean structure of the boundary layer, clouds, and precipitation along this 20° S transect, as deduced from measurements taken on the two long-range REx aircraft during numerous flights along 20° S supplemented by other relevant REx airborne, ship and surface observations. This expands upon composite thermodynamic transects along 20° S based on REx data and prior ship observations by Rahn and Garreaud (2010a). A companion paper by Allen et al. (2010) analyzes aerosol and chemical measurements along the 20° S transect.

ACPD
10, 15921–15962, 2010

Our presentation has been designed for comparison with monthly-mean climatology from regional and global weather, chemical transport and climate models. Even in the heart of the subtropical trade winds, there is also important variability on daily to weekly timescales, as well as a pronounced diurnal cycle. For the REx period, these are more fully discussed and compared with a regional model by Rahn and Garreaud (2010b).

2 Sampling and data sources

We will use a variety of "20° S" measurements taken within 1° latitude of 20° S during 16 October–15 November 2008. Figure 1 shows the longitude bands and time ranges sampled by the major REx platforms in this 20° S region. In this plot, the sampling time is indicated by color shading, darkest at night and lightest during the mid-day and afternoon.

The backbone of our analysis is a suite of measurements by the two VOCALS long-range aircraft, the NSF C130 and the UK BAe146. These are supplemented by in-cloud leg mean droplet concentration measurements from two shorter range aircraft, the Office of Naval Research Twin Otter and the Department of Energy G-1, rawinsonde profiles of basic thermodynamic variables and winds from the research vessel *Ronald H. Brown* (hereafter the *Brown*) and the REx coastal radiosonde site at Iquique (20.3° S, 70.1° W), vertical profiles from the Twin Otter, and dropsondes from four BAe146 flights. Together these provide remarkably comprehensive sampling along 20° S between 70–85° W, encompassing much of the climatological east-west extent of the Southeast Pacific stratocumulus regime. The airborne platforms mostly sampled between the pre-dawn hours and mid-afternoon. The C130, *Brown*, and Iquique data used in this paper are publically available in the National Center for Atmospheric Research (NCAR) Environmental Observing Laboratory (EOL) VOCALS data archive (http://www.eol.ucar.edu/projects/vocals/), except for University of Wyoming cloud radar/lidar data products that are still under development. We used BAe146 and G-1 data processed by the University of Manchester and Twin Otter data

ACPD
10, 15921–15962, 2010
VOCALS-REx 20 S boundary layer, clouds and precipitation
C. S. Bretherton et al.

processed by the University of Miami.

The C130 and BAe146 measurements were mostly taken while flying the 20° S survey pattern. Figure 2 shows an example, C130 flight RF03. The aircraft altitude is shown as the grey line overlaid on airborne radar/lidar measurements to be discussed later. Each repeat of this pattern samples the boundary layer, cloud, and lower free-tropospheric structure. It included a repeated sequence of three 60 km level legs including an above-cloud leg at 100–300 m above the capping inversion, an in-cloud leg flown near the middle of the stratocumulus layer (or slightly under the inversion in the absence of stratocumulus), and a subcloud leg flown at 150 m above sea level, typically interspersed with a deep profile to 3 km altitude after every other repetition of the leg sequence.

Four C130 flights on 21, 23, 25 October, and 6 November, and six BAe146 flights on 26, 29, 31 October, and 4, 9, 13 November, were dedicated to the 20° S pattern. In these flights, the aircraft took off from Arica, Chile (18° S, 70° W), flew to Point α (20° S 72° W), sampled westward exactly along 20° out to a maximum range, then returned along the same track. The C130 flew out past 85° W, and the BAe146 flew out to about 80° W. C130 flight RF05 added a short pattern near 20° S 85° W above the *Brown* for measurement intercomparisons. The BAe146 flights on B412 and B420 returned at 6 km altitude, dropping sondes roughly every 100 km.

In addition, the 20° S pattern was flown on portions of other flights, typically on a transit to or back from a pocket of open cells, sometimes but not always exactly along 20° S. Flight legs within 1° latitude of 20° S from such cases are included in this study. These include 1000+ km long segments of C130 flights on 18 October, 2, 13 and 15 November, and shorter segments of four other C130 flights and four other BAe146 flights. In total, parts of 12 C130 and 11 BAe flights sampled out to 80° W using the 20° S pattern, and 4 C130 flights reached 85° W.

The four dedicated C130 20° S flights sampled from 06:00–15:00 UTC. In the sampling region, sunrise was around 11:00 UTC so the outbound legs were entirely nocturnal, while the return legs sampled the initial morning evolution of the boundary layer.

The C130 flights on 18 October and 13 and 15 November sampled along 20° S from 13:00–16:00 UTC (morning to midday). The BAe146 flights typically spanned the range 09:30–15:30 UTC. As a result, near the coast there was extensive 20° S sampling during both the pre-dawn and late morning. Further offshore the sampling was weighted to around 12:00 UTC (post-dawn), with three flights providing midday coverage. Hence, our measurements must be interpreted in light of the strong daytime stratocumulus thinning typical of most days in this region.

The *Brown* soundings, taken every 4 h, span 3 days at 85° W, 3 days in transit to 75° W, 7 days at 75° W, and 2 days in transit between Arica and 75° W, as shown in Fig. 13 of Wood et al. (2010). Six soundings were made daily at Iquique throughout the entire period. The Twin Otter flew 18 missions between 16 October and 13 November from Iquique to Point α, where it made a daily profile and intensively sampled in the altitude range below 2 km. Of these profiles, 15 were made near 12:00 UTC and 3 were later, between 15:00–16:10 UTC.

Figure 3 shows daily "strip charts" of Geostationary Operational Environmental Satellite (GOES) 12 µm infrared brightness temperature at 08:45 UTC (pre-dawn) over the period 16 October–15 November 2008, based on a regional data subset assembled by NCAR/EOL and included in their VOCALS data archive. The missions and days with substantial C130 and BAe146 20° S sampling are indicated on the figure. These days span a representative set of days during this period, ranging from nearly solid cloud cover across the entire section from 70–90° W (18 October, 13 November) to much more broken conditions (25 October). Some broken cirrus (yellow) was present on about half the missions. Grey shading variations in the low clouds reflect inversion height fluctuations, with white indicating a deeper inversion and colder cloud tops. For instance, on 23 October there is a strong gradient toward colder cloud tops at 80° W than near the coast, while on 18 October and 13 November, there is little east-west cloud top temperature gradient.

ACPD
10, 15921–15962, 2010

VOCALS-REx 20 S boundary layer, clouds and precipitation

C. S. Bretherton et al.

3 Results

3.1 Thermodynamic profiles along 20° S

Figure 4 shows representative thermodynamic profiles from Iquique rawinsondes at 70° W and from C130 observations near 75, 80 and 85° W. For Iquique, the potential temperature θ and the water vapor mixing ratio q are plotted. The C130 profiles are of their moist-adiabatically conserved variants, liquid water potential temperature $\theta_l = \theta(1 - Lq_l/c_p)$ and $q_t = q_v + q_l$, where q_l is liquid water content (LWC) measured by a Gerber probe.

Near the coast, the temperature inversion that invariably caps the boundary layer in this region is typically near 1 km. At Iquique, there is a strong diurnal cycle with slope flows that can diffuse the inversion structure. Slightly offshore (e.g. at 75° W) the inversion is near to 1200 m, sharp, and strong (10–12 K), and the boundary layer is usually fairly well mixed. Further offshore, the inversion remains strong and typically sharp, but its height becomes somewhat more variable and usually deeper. When the boundary layer is deeper it is also more decoupled (Zuidema et al., 2009). If we diagnose decoupling as a humidity difference of more than 0.5 g kg^{-1} between the bottom of the profiles and the base of the cloud layer, all of the plotted 85° W profiles are decoupled.

At Iquique, there is often very complex layering of humidity and static stability above the inversion, which sometimes extends out past 75° W. Further offshore, occasional moist layers interleave with extremely dry air with mixing ratios as low as 0.1 g kg^{-1}.

3.2 Multiplatform 20° S monthly-mean vertical sections

By combining observations from Iquique, the *Brown*, the C130 (in-situ observations), BAe146 (dropsondes only), and Twin Otter (profiles on each flight at 20° S, 72° W), we have sufficient longitude and time sampling to build up time-mean 20° S cross-sections of temperature, humidity and winds for the month 16 October–15 November (Julian days 290–320). These are calculated in 2.5° longitude and 100 m height bins, and will be available from the VOCALS EOL data archive. The 2.5° bin size is chosen because each aircraft mission includes enough sampling within and above the boundary layer in this longitude increment to provide a meaningful profile. Since different platforms had different observational strategies, we weight the profiles so that all observations from a single platform on a single day in a single longitude bin are averaged into a single binned profile with unit weight. This is a crude way to account for serial correlation, using a nominal decorrelation time of a day and lengthscale of 2.5°. Thus, each of the six-daily Iquique and *Brown* soundings are given a weight of 1/6, and the BAe146 dropsondes, which are usually 1° longitude apart, are given a weight of 2/5. Each C130 flight contributes a weight of 1 for those longitude and height bins which it samples; outbound and inbound legs from the same flight are combined for this purpose. The profile from each Twin Otter flight is also given a weight of 1.

For each profile, the "RH-inversion" is diagnosed as the lowest height for which the relative humidity (RH) is less that 45%. This threshold is empirically chosen to be lower than the RH ever observed within the boundary layer, but higher than the RH ever observed above the boundary layer in this region (except for one Iquique sounding, for which the RH-inversion was identified by eye). The inversion base is then defined as the height of minimum temperature below the RH-inversion. The inversion base and its temperature should correspond closely to the cloud top of any nearby stratocumulus. For each longitude bin, platform-weighted 25, 50 and 75th percentiles of inversion base were calculated, as well as the overall minimum and maximum inversion height.

3.3 Monthly-mean 20° S temperature and humidity cross-sections

Figure 5 shows the resulting monthly-mean cross-sections of temperature T and water vapor mixing ratio q_v. At the top of the temperature section, colored rectangles show the average sample frequency for each platform (the weighted number of samples at the inversion height divided by the 31 days of the month). This shows excellent sampling east of 80° W, with sparse sampling further offshore, where only the C130 and

ACPD
10, 15921–15962, 2010

the *Brown* took measurements. In the two easternmost longitude bins, the weighted number of samples marginally exceeds 31 because multiple platforms sometimes sampled the same bin on the same day; the rectangle widths at the top of those bins are rescaled to sum to the bin width.

This one-month mean section should not be interpreted as a monthly climatology, although balloon soundings from the *Brown* in previous years (De Szoeke et al., 2010; Rahn and Garreaud, 2010a) suggest it is broadly representative and could be used to identify all but the most subtle biases in a climate model.

The near-surface air temperature is nearly constant across the section, echoing the sea-surface temperature (SST) distribution shown along the bottom of the section. The SST is the longitude-binned average of Reynolds SST within 0.25° latitude of 20° S for this period. Radiometric SST measurements from the C130 closely tracked Reynolds SST after subtracting a uniform −1 K offset from the former.

There is a systematic westward drop in free tropospheric temperature that helps explain why the inversion deepens to the west. The median inversion height increases from 1000 m at the coast to 1600 m at 85° W. On occasion, the inversion height ranged from less than 1 km to more than 2 km at 85° W, and at Iquique, a similarly large range from 500–1600 m was seen, but the middle quartile of inversion heights show a remarkably narrow spread at all longitudes. This is why the inversion sharpness is quite well preserved in the mean T cross-section.

In comparing this cross-section with coarse-resolution model simulations, one should be aware within 300 km of the coast, the inversion height is strongly affected by regional features of the South American coastline. Satellite-derived maps show that October climatological cloud-top height ranges from less than 800 m at 25° S, where there are strong coastal southerlies, to more than 1300 m in parts of the Arica Bight at 17–18° S, where the southerly flow is blocked (Zuidema et al., 2009).

The near-surface humidity is also fairly constant across the cross-section. The apparent variations may reflect differences between the airborne and balloon humidity sensors as much as they reflect true humidity differences. The vertical moisture gradi-

ACPD
10, 15921–15962, 2010

ents in the boundary layer are small near the coast (indicating a climatologically well-mixed structure) but larger west of 80° W where the boundary layer is usually decoupled.

Near the coast, the mean free tropospheric mixing ratio is 2–3 $g\,kg^{-1}$. Over the west slopes of the Andes, moist boundary layer air is mixed into the free troposphere. Sometimes this moist air then advects offshore out to 75–80° W before subsiding into the inversion. During other synoptic regimes, the moist air is trapped along the coast. The air subsiding to the west is usually very dry, typically 0.1–1 $g\,kg^{-1}$ in the above-cloud legs. Back-trajectories suggest that it has come from the South Pacific Convergence Zone or the South Pacific midlatitude storm track.

These dynamics build in a natural correspondence between free-tropospheric aerosol concentrations, humidity and temperature that must be carefully considered when interpreting correlations between cloud properties and aerosols.

3.4 Monthly-mean 20° S wind cross-sections

Figure 6 shows multiplatform 16 October–15 November 2008 mean cross-sections of the wind components u and v along 20° S. There is strong horizontal divergence of u across the cross-section in both the boundary layer and free troposphere. Further offshore, the mean v strengthens in the boundary layer and reverses from northerly near the coast to southerly west of 78° W. Within the boundary layer both wind components are relatively uniform with height. Between 71 and 79° W, there are sharp jumps of the mean u and v of up to 5 $m\,s^{-1}$ across the mean inversion height.

Even at the low latitude of 20° S, the wind is broadly geostrophic both in and above the marine boundary layer. A mean east-west slope $\partial z_{inv}/\partial x$ of the sharp inversion temperature jump ΔT will induce a geostrophic meridional velocity jump Δv_g across the inversion:

$$f \Delta v_g \approx -(g/T_{ref})\Delta T \partial z_{inv}/\partial x\,, \tag{1}$$

where g is gravity, $f = -5\times10^{-5}\,s^{-1}$ is the Coriolis parameter at 20° S, g is gravity, and

ACPD
10, 15921–15962, 2010

Title Page
Abstract | Introduction
Conclusions | References
Tables | Figures
◀| |▶
◀ ▶
Back | Close
Full Screen / Esc
Printer-friendly Version
Interactive Discussion

T_{ref}=285 K is a characteristic temperature at the inversion height. Between 71 and 79° W, the mean inversion slope observed during REx along 20° S was −0.5 m km^{-1}. Taking $\Delta T \approx 10$ K, the implied inversion jump is $\Delta v_g \approx -4$ m s^{-1}, which is comparable to the observed inversion jump Δv . A satellite analysis for October 2008 given in Fig. 11 of Zuidema et al. (2009) suggests that along 20° S, the inversion slopes downward to the north at about 1 m km^{-1} between 71 and 79° W. This implies a geostrophic zonal wind jump $\Delta u_g \approx 8$ m s^{-1} across the inversion. This is even stronger than the observed zonal wind jump; surface drag may reduce the easterly wind component in the boundary layer and hence the zonal wind jump.

3.5 Comparison of 20° S leg-mean winds with operational analyses

Trajectory analysis is a central interpretive tool for interpreting REx chemical and aerosol measurements. It relies on gridded winds from large-scale analyses. The surface winds in analyses are constrained by scatterometer measurements, but model-analyzed winds in the lower free-troposphere in the VOCALS region may be more affected by forecast model error due to the lack of constraining observations. This raises doubts about the reliability of trajectories computed for the VOCALS region, especially above the boundary layer.

To address this issue, we compare the winds forecast by two analyses against the C130 and BAe146 leg-mean winds for all 20° S subcloud and above-cloud legs. Using leg-mean winds greatly reduces potential scatter associated with 10–30 km wide mesoscale open-cell and closed-cell boundary-layer circulations that are ubiquitous in this region. We expect that the agreement with analyses will be better for the subcloud legs, which are near the surface, than for the above-cloud legs. We do not include the cloud legs in this analysis, because they are typically within 100 m below the inversion base, and the model-analyzed winds at this level may be sensitive to small errors in inversion height or under-resolution of the inversion.

We use the operational global analyses from the National Centers for Environmental Prediction (NCEP; their “FNL” analysis) and the European Centre for Medium-Range

ACPD
10, 15921–15962, 2010

Title Page
Abstract | Introduction
Conclusions | References
Tables | Figures
◂ | ▸
Back | Close
Full Screen / Esc
Printer-friendly Version
Interactive Discussion

Weather Forecasts (ECMWF), which are both commonly used for trajectory analysis. Each analysis is interpolated to the central latitude, longitude, altitude and time of the corresponding leg. Figure 7 shows scatterplots of the FNL and ECMWF wind components vs. their observed counterparts, color-coded into subcloud (red) and above-cloud (blue) legs. Both analyses are remarkably accurate, with a rms error of roughly 1 m s^{-1} for the subcloud legs and 2 m s^{-1} for the above-cloud legs. The subcloud leg errors are consistent with a comparison of ECMWF/NCEP and scatterometer-derived near-surface winds (Chelton and Freilich, 2005).

The NCEP reanalysis, also commonly used for trajectory calculation, does not compare as well with the 20° S observations, especially for v, with rms wind errors exceeding 3 m s^{-1} both in and above the boundary layer. In particular, it tends to produce excessive near-surface southerlies between 75–80° W. This may reflect a model bias (associated with too strong a westward inversion slope) inadequately removed by observations, as well as the coarse 2.5° resolution of our gridded reanalysis fields. Thus, we strongly recommend use of the NCEP FNL or ECMWF operational analyses over the NCEP reanalysis for computing trajectories in the VOCALS region.

3.6 Back-trajectories

Figure 8 shows back-trajectories from NCEP FNL operational analyses for 12:00 UTC on the C130 20° S mission days. The top panels show 3-dimensional two-day back-trajectories originating at 850 hPa from 85° W and 75° W, representative of the free-tropospheric air subsiding into the boundary layer. The bottom panels show corresponding 2-dimensional isobaric back-trajectories at 950 hPa, representative of boundary-layer air.

The 75° W boundary layer back-trajectories come from the south, typically passing within 300 km of the Chilean coast at 33° S, the latitude of Santiago. The 75° W free-tropospheric back-trajectories are quite diverse. Free-tropospheric coastal northerlies frequently extend out to 75° W, bringing down air from the Peruvian coastal region. Trajectories switch to the south and west and exhibit stronger subsidence after the passage of upper-level troughs. We conclude that out to 75° W, the marine boundary layer has usually been influenced by coastal anthropogenic aerosol sources, with intermittent influence of South American aerosol sources on the subsiding free-tropospheric flow.

At 85° W, the 2-day back-trajectories both in and above the boundary layer are from the southeast, but stay too far offshore to permit much influence of South American emissions, at least at the plotted times.

3.7 Cloud droplet and accumulation-mode aerosol and cconcentrations

During REx, three aircraft (the C130, BAe146, and Twin Otter) made extensive airborne measurements of cloud droplet concentration N_d along 20° S. A fourth aircraft, the G-1, mainly sampled N_d north of 20° S but also sampled with 1° latitude of 20° S on three days. These measurements form a central link in relating aerosol and cloud properties and in testing satellite retrievals of N_d over the VOCALS region.

We computed a cloud leg-mean N_d averaged over those periods during the leg in which the LWC exceeded 0.05 g m^{-3} (C130 and BAe146) or by using only in-cloud legs with mean LWC greater than 0.05 g m^{-3} (G-1 and Twin Otter). This threshold was chosen to avoid averaging in cloud-free air, which could induce a low bias in N_d. On both the C130 and BAe146, N_d was measured at 1 Hz with a Particle Measurement Systems (PMS) Cloud Droplet Probe, except for C130 flights RF03 and RF04, when that probe was not working and a PMS Forward Scattering Spectrometer Probe (FSSP-100) was used instead. Comparisons from the other C130 flights suggest the CDP and FSSP concentrations were very similar, adding credibility to both measurements. On the G-1 and Twin Otter, droplet concentrations were measured using a Cloud and Aerosol Sampling (CAS) probe, which detects a somewhat broader range of particle sizes (0.6–60 µm) than the other probes.

We compared these measured N_d with daily satellite retrievals at approximately 15:30 UTC (late-morning local time) using the Moderate Resolution Imaging Spectrometer (MODIS; http://modis.gsfc.nasa.gov/) on Terra, following the method of Bennartz

Discussion Paper | Discussion Paper | Discussion Paper | Discussion Paper |

ACPD
10, 15921–15962, 2010

VOCALS-REx 20 S boundary layer, clouds and precipitation

C. S. Bretherton et al.

(2007), as detailed in George and Wood (2009). These retrievals are based on MODIS-observed visible optical depth and effective radius in regions with cloud fraction greater than 0.8, and they have been averaged over $1^\circ \times 1^\circ$ gridboxes.

Figure 9 shows a longitude-time plot of 20° S N_d over 16 October–15 November 2008. The aircraft measurements (colored symbols) extensively sample the region east of 80° W throughout the month. The MODIS retrievals (color-shaded boxes) are generally consistent with the aircraft measurements, showing similar patterns of longitudinal and temporal variability. The correlation coefficient between the aircraft N_d and the satellite N_d from the nearest gridbox and time is 0.77, based on the 125 collocations (out of 140 total) for which the MODIS cloud fraction exceeded 0.8. Across these collocations, the mean aircraft $N_d = 164\,\text{cm}^{-3}$ compares favorably with the mean MODIS $N_d = 142\,\text{cm}^{-3}$. Because droplet concentration sometimes has sharp gradients (e.g. around POCs) that advect across 20° S, and because the satellite overpasses may be up to eight hours offset from the corresponding aircraft measurments, perfect agreement is not expected. The results shown in Fig. 9 support the use of high-quality satellite retrievals to quantify space-time variability of N_d in subtropical stratocumulus regions.

Figure 10 shows a monthly-mean perspective on N_d and its relationship to accumulation-mode aerosol. The aircraft measurements in Fig. 9 over the month are binned into three longitude ranges, nearshore (70°–75° W), transitional (75°–80° W) and remote (80°–85° W). Within each longitude range, the leg-mean N_d measurements for each aircraft (except the G-1, for which we don't have enough 20° measurements) are plotted using a boxplot (box-whisker) format to show temporal and small-scale spatial variability. Each box shows the median, interquartile range, and extremes of the measured quantity (N_d in this case) over the flight legs in that longitude bin. The same is done for the accumulation-mode (0.1–3 µm diameter) aerosol concentration averaged across C130 subcloud legs, as measured by the PMS Passive Cavity Aerosol Spectrometer Probe (PCASP). The numbers of contributing 60 km flight legs are shown at the top of each box.

Discussion Paper | Discussion Paper | Discussion Paper | Discussion Paper |

ACPD

10, 15921–15962, 2010

The solid line is the MODIS average N_d for 16 October–15 November 2008. The agreement between the mean satellite N_d and the corresponding aircraft observations is impressive. Both the data and the climatology show that droplet concentrations typically exceed 200 cm^{-3} near the coast and drop below 100 cm^{-3} west of 80° W. There is pronounced variability in droplet concentration in the transition zone, as seen by the larger interquartile range than in the nearshore and remote zones.

PCASP concentrations usually exceeded 200 cm^{-3} east of 75° W (within 500 km of the Chilean coast), but rarely exceeded 300 cm^{-3} further offshore. At all longitudes, PCASP concentrations ranged over a large range between flights due to synoptic variability in the air flow. At any given longitude, there is not a strong correlation between PCASP and cloud droplet concentrations, but on average, N_d is 80% of the PCASP concentration except in the remote region, where it is only 50%.

4 Cloud radar and lidar observations

The University of Wyoming 94 GHz cloud radar (WCR) and upward-pointing lidar (WCL) aboard the C130 provided valuable sampling of clouds and precipitation to complement in-situ measurements. For an example, we return to Fig. 2, which shows the cloud radar reflectivity between 73–85° W during a typical early-morning C130 20° S mission, RF03. Using both downward and upward-pointing radar beams, radar reflectivity was profiled throughout the flight outside an 80 m dead zone around the aircraft. During subcloud legs, the flight-level lifting condensation level (LCL) and the cloud base inferred from the upward-pointing lidar are also shown. During in-cloud legs, the cloud base inferred adiabatically from the in-situ LWC is shown.

Several typical features can be seen in Fig. 2. East of 75° W, there is cloud but radar echoes are weaker than −15 dBZ, indicating almost no drizzle-size droplets. West of 75° W, stronger cellular radar echoes extending well below cloud base, indicating drizzle, are widespread. Occasional echoes reach 20 dBZ, but most of the echoes are less than 10 dBZ and do not reach the sea-surface, suggesting nearly complete evaporation

ACPD
10, 15921–15962, 2010

of the drizzle in agreement with EPIC 2001 shipborne observations at 20° S 85° W. In the nearshore region, the LCL and cloud base are both close to 900 m, implying a well-mixed boundary layer. The inversion and cloud base deepen to the west, but the LCL does not, showing a transition from a well-mixed to less well-mixed boundary layer. Both the cloud base and LCL also become more variable further offshore, lowering in the cores of drizzle cells (high radar reflectivity).

Using analogous measurement from all the C130 20° S flight legs, we can assemble a statistical view of cloud properties and precipitation. Figure 12 shows a longitude-binned boxplot of the radar cloud top, the lidar cloud base, and the LCL. The median cloud top lies at the inversion base, and its leg-to-leg variability is due mainly to day-to-day inversion base variations. The bin-median cloud base is around 1000 m in the nearshore and transitional bins, rising to 1200 m in the remote bin. The bin-median LCL lies between 900 and 1000 m in all bins; the increased difference between median LCL and median cloud base in the remote region is a statistical indicator of a more decoupled boundary layer structure.

Figure 12 shows longitude-binned boxplots of subcloud leg fractions of cloud cover, "scud", and heavy cloud-base drizzle derived from the WCL and WCR. Cloud fraction was calculated as the leg-average of a 1 Hz cloud occurrence indicator derived from the WCL. Scud (another indicator of decoupling) was defined as a 1 Hz cloud base more than 100 m below the leg-median cloud base, and heavy cloud-base drizzle was defined as a column-maximum WCR reflectivity exceeding 0 dBZ. At all longitudes, the majority of legs were nearly 100% cloud covered. In the nearshore bin, scud was seen less than half the time, while some scud was seen on all legs in the remote bin. Drizzle exceeding 0 dBZ was not observed in the nearshore legs, but was observed on over 75% of the remote legs, with up to 90% coverage within the drizzliest leg.

From the difference between WCL cloud base and WCR cloud top, a 1 Hz adiabatic LWP can be derived during all the subcloud legs (Fig. 13). Microwave measurements of LWP were also made on the C130, but are only processed for a few flights at present. They usually closely agree with the adiabatic LWP (Zuidema 2009, personal commu-

Discussion Paper | Discussion Paper | Discussion Paper | Discussion Paper |

ACPD

10, 15921–15962, 2010

VOCALS-REx 20 S boundary layer, clouds and precipitation

C. S. Bretherton et al.

nication), as also found by Bretherton et al. (2004). For each leg, Fig. 13 shows the interquartile range as well as the median LWP, emphasizing the large mesoscale variability in LWP. In the remote region, the adiabatic LWP is more variable (both between legs and within legs) and typically larger than in the nearshore region. High leg-median LWP legs in the remote region had copious drizzle and pronounced mesoscale variability – up to a factor of 7 between the 25th and 75th percentiles of LWP. There are not enough samples to pick out any clear difference between predawn and mid-morning LWP.

Since large-scale models predict drizzle rather than radar reflectivity, we made estimates of the longitude-binned leg-mean rain rate at various levels using both radar and in-situ measurements with the raindrop size distribution from the PMS 2D-C probe on the C130, which detects and sizes droplets between 100 and 800 µm in diameter. The three radar-based estimates are based on the 1 Hz column-maximum radar reflectivity Z_{max}, the reflectivity Z_{500} at 500 m altitude and the reflectivity Z_{100} at 100 m (this is the closest height to the sea-surface for which the reflectivity can be reliably separated from the surface echo in all legs). We interpret Z_{max} as representative of the local cloud base in situations in which there is significant drizzle (noting that Z_{max} may occur higher in the cloud layer when drizzle is weak or absent), and we use Z_{100} to obtain a surface rain rate proxy.

Some salient aspects of the WCR data are as follows. The radar beam was split into upward and downward components (giving Z_{max}, Z_{500}, and Z_{100}) except on the subcloud legs, when only the upward beam was used so Z_{100} was not measured. No attenuation correction was applied; this may bias Z_{100} low by a few dBZ when the aircraft was flying through or above a heavily drizzling cloud. In cloud legs, the true reflectivity maximum may lie within the radar dead zone and be larger than the measured Z_{max}.

We convert Z_{max} and Z_{500} into estimated rain rates R_{max} and R_{500} [mm d^{-1}] using the cloud-base $Z-R$ relationship inferred by Comstock et al. (2004), while using their

Discussion Paper | Discussion Paper | Discussion Paper | Discussion Paper |

ACPD

10, 15921–15962, 2010

VOCALS-REx 20 S boundary layer, clouds and precipitation

C. S. Bretherton et al.

surface $Z-R$ relationship on Z_{100}:

$$Z_{max} = 25(R_{max}/24)^{1.3}, \quad (2)$$

$$Z_{500} = 25(R_{500}/24)^{1.3}, \quad (3)$$

$$Z_{100} = 57(R_{100}/24)^{1.1}. \quad (4)$$

The Comstock et al. cloud base and surface $Z-R$ relationships are consistent with our 2D-C drop spectra from in-cloud and subcloud legs, respectively, and they were derived at 20° S 85° W, giving us confidence in these rain rate estimates. However, all $Z-R$ rainfall estimates have substantial uncertainty and even their bin-mean values should be considered uncertain within a factor of two, even before considering possible attenuation biases.

We leg-average these rain rate estimates from all subcloud, in-cloud and above-cloud C130 legs; their longitude-binned statistics are shown in Fig. 14. The figure shows statistics for the cloud and subcloud (150 m) leg-mean 2D-C rain drop size spectra converted to precipitation fluxes using a standard droplet radius-fall speed relationship (Pruppacher and Klett, 1997). This estimate deliberately does not include the sedimentation of cloud droplets, which are generally much smaller than the 100 µm minimum diameter detected by the 2D-C. Since the leg-mean rainfall has a very skewed frequency distribution, we also show the all-leg means for each longitude range as colored dots.

The highest rainfall estimates come from Z_{max}; these estimates are reassuringly consistent with the 2D-C in-cloud estimates. Both approaches show that rainfall rates in the nearshore longitude band are usually very small, but increase dramatically in the remote region, with intermediate results in the transition region. In the remote region, almost 50% of legs have a leg-mean rain rate exceeding 1 mm d^{-1} by either of these measures, and the overall average in-cloud/cloud base rain rate is 1–2 mm d^{-1}.

Several recent studies have related area-averaged cloud base rain rate to LWP and N_d, and forthcoming REx studies will also address this issue. The Comstock et al. fit, based on ship observations in SE Pacific stratocumulus from EPIC2001, found cloud

Discussion Paper | Discussion Paper | Discussion Paper | Discussion Paper |

ACPD
10, 15921–15962, 2010

VOCALS-REx 20 S boundary layer, clouds and precipitation

C. S. Bretherton et al.

base rain rate goes as $(\mathrm{LWP}/N_d)^{1.75}$. This suggests that the westward increase in rain rate is due in similar measure to LWP (typically twice as large in the remote region as the nearshore region) and N_d (a factor of 2–3 smaller in the remote region); together these imply a mean cloud base rain rate which is a factor of 10–20 larger in the remote region, compared to the observed factor of 50. The N_d gradients are probably partly anthropogenic, but the LWP gradients probably are associated with the increasing depth and changed vertical structure of the boundary layer further offshore. Thus, even without anthropogenic aerosol perturbations, it seems plausible that cloud base drizzle would be much larger in the remote SE Pacific than in the coastal zone.

During EPIC 2001, ship-based measurements were used to estimate that 85% of the cloud-base rain evaporated before reaching the surface. Our airborne measurements from REx corroborate this conclusion. In the remote region, the mean 100 m radar-derived rain rate is only 0.04 mm d^{-1}, only two percent of the cloud-base estimate. The 2D-C rain rate at 150 m gives a less extreme picture that is more consistent with the EPIC2001 estimates. The mean 2D-C 150 m rain rate is dominated by one leg and seems unrepresentative. We focus instead on the 75th percentile of leg-average rainrate (the upper edge of the red box), which should be more statistically robust and is close to the mean precipitation over the larger set of radar legs (the black, green and pink boxes). The 75th percentile of the 2D-C 150 m rain rate estimate is 0.2 mm d^{-1} in the remote region, five times as large as the radar estimate and about 15% of the 2D-C in-cloud estimate. This suggests that an attenuation correction may be needed to reliably estimate mean surface rainfall from the WCR Z_{100}. A 5–7 dBZ attenuation correction to Z_{100} in the heaviest drizzle events, which we have calculated is quite plausible, would suffice to obtain consistency with the 2D-C rain rate estimates. In the meanwhile, the 75th percentile of the 150 m 2D-C rain rates are our best guess at the mean surface rain rate in each longitude bin.

The 500 m radar rain rates are, as expected, intermediate between the near-surface and in-cloud values. On average, they are almost a factor of ten larger than their near-surface counterparts. While this is probably an overestimate due to attenuation, it is still

ACPD
10, 15921–15962, 2010

a remarkable testament to the effectiveness of subcloud drizzle evaporation. With an appropriate attenuation correction, the 20° S 500 m rain rate and its ratio to surface rain rate would make an interesting test of the microphysical parameterizations in large-scale models, building on results in a GEWEX Cloud System Study single-column model intercomparison for a drizzling Northeast Pacific stratocumulus layer (Wyant et al., 2007).

5 Radiative driving and boundary layer turbulence

Turbulence in subtropical stratocumulus-topped boundary layers is strongly forced by cloud top longwave cooling, compensated by solar shortwave heating during the day. In this section we use C130 measurements to estimate the longwave flux divergence across the boundary layer and the intensity and gross vertical structure of the turbulence. The C130 20° S flight pattern, which did not attempt to collocate above-cloud and below-cloud legs and was biased toward night and early-morning flights, is not suitable for estimating daily-mean shortwave heating in the boundary layer. We find that both the longwave driving and the in-cloud turbulence are stronger further offshore.

5.1 Longwave driving of the PBL

The extraordinarily dry free troposphere sampled by the C130 west of 75° W (Fig. 5b) allows efficient longwave cooling of the cloud-topped boundary layer. A crude bulk estimate can be derived using the difference between the net upward broadband longwave flux in the above-cloud legs and the subcloud legs in a given longitude range. Figure 15 shows boxplots of the C130-measured flux components for the three longitude bins, and an estimated boundary-layer longwave flux divergence between the surface and the inversion.

Turning first to the above-cloud measurements, the average downwelling longwave flux drops from 240 W m^{-2} in the nearshore box to 200 W m^{-2} in the remote box, where

ACPD
10, 15921–15962, 2010

the lower free troposphere is drier and cooler. The upwelling longwave flux drops from 350 W m^{-2} in the nearshore box to 340 W m^{-2} in the remote box, where the cloud tops are higher and slightly colder. Thus, the net upward longwave flux at the above-cloud level is 110 W m^{-2} in the nearshore box, increasing to 140 W m^{-2} in the remote box.

The subcloud legs show a downwelling longwave flux of about 350 W m^{-2}, an upward flux of about 380 W m^{-2}, and hence a net upward longwave flux of roughly 30 W m^{-2} in all longitude bins.

To estimate a boundary layer radiative flux divergence from these measurements, we neglect longwave flux divergence between the sea surface and 150 m (since the overlying low cloud keeps the longwave cooling rate small). We estimate that on average there is 10 W m^{-2} of radiative flux divergence in the 300 m between the inversion and the above-cloud legs (an average longwave cooling rate of nearly 4 K d^{-1} in this layer). This leads to the estimates in Fig. 15 of the mean boundary layer longwave flux divergence in each longitude bin. The net boundary layer longwave cooling increases from 70 W m^{-2} in the nearshore box to 100 W m^{-2} in the remote region. These longwave cooling rates are mainly measured in the early morning, when cloud fraction is highest. In the afternoon, longwave boundary layer radiative flux divergence probably reduces somewhat as the cloud becomes broken.

Radiosondes from the *Brown*, e.g. during EPIC 2001 (Bretherton et al., 2004) show that free-tropospheric moist layers with mixing ratios up to 4 g kg^{-1} do sometimes occur even at 85° W. This is another reason that these C130 measurements may overestimate the mean boundary layer longwave cooling at 85° W. In fact, Caldwell and Bretherton (2005) estimated a 6-day mean boundary-layer longwave cooling of 78 W m^{-2} (and a shortwave warming of 26 W m^{-2}) at 85° W by applying a radiative transfer parameterization to EPIC 2001 cloud and radiosonde observations. Nevertheless, the typical dryness of the free troposphere clearly provides a favorable radiative environment for extensive and persistent stratocumulus well offshore.

ACPD
10, 15921–15962, 2010

5.2 Vertical velocity variance

Strong cloud-top radiative cooling should also lead to strong turbulence in the cloud layer beneath. Figure 16 shows boxplots of leg-mean vertical velocity variance for the 20° S in-cloud and subcloud C130 legs. There is considerable flight-to-flight variability, and a tendency for late-morning legs to be less turbulent than nighttime legs. However, the biggest signal is a 50% increase in the standard deviation of in-cloud w from the nearshore box to the remote box. This large offshore increase in turbulence is consistent with the stronger longwave driving. We cannot rule out an additional artificial contribution from systematic differences in the geometry of the flight legs as the C130. Because the nearshore clouds were thinner, the C130 typically flew closer its in-cloud legs to the inversion there, as compared to the remote region. Because vertical velocity variance rapidly decreases as the measurement height approaches the inversion height, this could artificially enhance the offshore increase in the standard deviation of w as measured from the in-cloud legs. However, the signal is so large that we believe that it seems unlikely to be dominated by this artificial bias.

No similar trend and little evidence of a diurnal cycle is seen in the subcloud (150 m) legs. Because the boundary layer is not well mixed west of 75° W, or even closer to the coast during the daytime, the cloud radiative forcing has little effect on 150 m turbulent vertical velocity variance; surface wind and air-sea temperature differences play larger roles.

6 Conclusions

VOCALS-REx observations provide an unprecedented comprehensive dataset along the 20° S transect documenting systematic gradients in clouds, precipitation and vertical structure across a major stratocumulus-topped boundary layer regime. The dataset extends from a polluted coastal zone to a deeper, more decoupled, lower-aerosol, drizzlier regime 1500 km offshore of Northern Chile. We have synthesized observations

ACPD
10, 15921–15962, 2010
VOCALS-REx 20 S boundary layer, clouds and precipitation
C. S. Bretherton et al.

from 4 REx aircraft spanning almost every day of the 16 October–15 November 2008 study period, complemented by soundings from the *Brown* and Iquique. The Wyoming cloud radar and lidar aboard the C130 provided a unique survey of the vertical structure and mesoscale variability of clouds and precipitation across the transect.

Consistent with satellite retrievals, aircraft-measured droplet concentrations ranged from 250 cm^{-3} near the coast to less than 100 cm^{-3} 1500 km offshore. Cloud droplet concentrations were correlated with accumulation-mode aerosol concentration in the subcloud layer. Aircraft-measured winds averaged over 60 km level flight legs compared remarkably well with operational analyses from NCEP and ECMWF both within and above the boundary layer, suggesting that such analyses are adequate to construct back-trajectories for interpreting in-situ aerosol and chemical measurements. Two-day back-trajectories from locations along the 20° S transect within the boundary layer showed that longitudes east of 75° W experience frequent influence from possible pollution sources along the Chilean coast, but west of 80° W the coastal influence becomes much more sporadic. Above the boundary layer, three-dimensional two-day back trajectories initiated along 20° S and west of 75° W showed little influence from South America.

Drizzle was rare with 500 km of the coast, but was both common and much more intense further offshore, with mean cloud-base drizzle rates of around 1 mm d^{-1}. As in the EPIC2001 measurements, 80–90% of the drizzle evaporated before reaching the surface. The offshore drizzle should not just be interpreted as a response to lower aerosol concentrations. Other macrophysical gradients appeared to play just as important a role during REx. The boundary layer deepened from an average of 1000 m near the coast to 1600 m offshore, becoming much more decoupled offshore with deeper clouds and more pronounced mesoscale variability in liquid water path. This appeared to contribute just as strongly as N_d gradients to the offshore drizzle enhancement.

The deepening of the boundary layer was in turn associated with gradients in free-tropospheric conditions along 20° S. Near the coast, Andean slope heating kept the lower free troposphere warm and mixed up moisture from the boundary layer. Further

ACPD
10, 15921–15962, 2010

offshore, the free troposphere was cooler and remarkably dry. This both reduced the capping inversion and enhanced the longwave cooling, driving stronger turbulence in the cloud layer. Both factors supported stronger entrainment and a deeper boundary layer offshore.

We intend to make extensive use of the 20° S transect dataset for the VOCALS Assessment (VOCA), a model intercomparison for regional and global weather, chemical transport, and climate models. This is a follow-on to the PreVOCA study (Wyant et al., 2010), which was based on model simulations for October 2006 tested against satellite data and observations from prior NOAA cruises to the region. VOCA is particularly aimed at using the SE Pacific as a testbed for climate model simulations of chemical transport and aerosol cloud interaction.

Acknowledgements. The authors gratefully acknowledge support from NSF grants ATM-0745702 (CB and RW) and ATM-0745986 (DL) and NOAA Award NA07OAR4310282 (RG). UK financial support (GA and the BAe146 group) was provided by the National Environment Research Council Grant number NE/F019874/1. The RAF C130 measurements, *Brown* and Iquique soundings were obtained from the VOCALS data archive of NCAR/EOL, which is sponsored by the National Science Foundation. The *Brown* sounding dataset was synthesized by Simon deSzoeke. The Brookhaven G-1 group generously provided in-cloud observations from which we extracted cloud droplet concentrations. We also acknowledge Chris Terai for helping prepare C130 profiles, Andrew Berner for processing Reynolds SSTs, Keith Bower, Hugh Coe, James Dorsey and Martin Gallagher for their scientific direction of the BAe146, the staff at FAAM, DirectFlight and Avalon for supporting the provision of the BAe146, the staff of the U. Wyoming King Air National Facility who supported the deployment of the WCR and WCL, and the many other VOCALS-REx personnel whose efforts led to a remarkably comprehensive set of 20° S observations.

ACPD

10, 15921–15962, 2010

References

Allen, G., and Coe, H., Bretherton, C. S., and coauthors: Aerosol and trace gas measurements in the South East Pacific during Austral spring, Atmos. Chem. Phys. Discuss., to be submitted, 2010. 15923

Bennartz, R.: Global assessment of marine boundary layer cloud droplet number concentration from satellite, J. Geophys. Res., 112, D02201, doi:10.1029/2006JD007547, 2007. 15933

Bretherton, C. S., Uttal, T., Fairall, C. W., Yuter, S., Weller, R., Baumgardner, D., Comstock, K., and Wood, R.: The EPIC 2001 stratocumulus study, B. Am. Meteorol. Soc., 85, 967–977, 2004.

Caldwell, P., Bretherton, C. S., and Wood, R.: Mixed-layer budget analysis of the diurnal cycle of entrainment in Southeast Pacific stratocumulus, J. Atmos. Sci., 62, 3775–3791, 2005.

Chelton, D. B. and Freilich, M. H.: Scatterometer-based assessment of 10-m wind analyses from the operational ECMWF and NCEP numerical weather prediction models, Mon. Weather Rev., 133, 409–429, 2005. 15932

De Szoeke, S. P., Fairall, C. W., Wolfe, D. E., Bariteau, L., and Zuidema, P.: Surface flux observations on the Southeastern Tropical Pacific Ocean and attribution of SST errors in coupled ocean-atmosphere models, J. Climate, 23, doi:10.1175/2010JCLI3411.1/2010JCLI3411.1, 2010. 15929

George, R. C. and Wood, R.: Subseasonal variability of low cloud radiative properties over the southeast Pacific Ocean, Atmos. Chem. Phys., 10, 4047–4063, doi:10.5194/acp-10-4047-2010, 2010. 15934

Pruppacher, H. R. and Klett, J. D.: *Microphysics of Clouds and Precipitation*, 2nd edition, Kluwer Academic Publishers, Dordrecht, 954 pp., 1997. 15938

Rahn, D. A. and Garreaud, R.: Marine boundary layer over the subtropical southeast Pacific during VOCALS-REx – Part 1: Mean structure and diurnal cycle, Atmos. Chem. Phys., 10, 4491–4506, doi:10.5194/acp-10-4491-2010, 2010a. 15923, 15929

Rahn, D. A. and Garreaud, R.: Marine boundary layer over the subtropical southeast Pacific during VOCALS-REx – Part 2: Synoptic variability, Atmos. Chem. Phys., 10, 4507–4519, doi:10.5194/acp-10-4507-2010, 2010b. 15924

Wood, R., Bretherton, C. S., Mechoso, C. R., and coauthors: The VAMOS Ocean-Cloud-Atmosphere-Land study regional experiment (VOCALS-REx): goals, platforms and field operations, Atmos. Chem. Phys. Discuss., to be submitted, 2010. 15926

ACPD

10, 15921–15962, 2010

VOCALS-REx 20 S boundary layer, clouds and precipitation

C. S. Bretherton et al.

Wyant, M. C., Wood, R., Bretherton, C. S., Mechoso, C. R., Bacmeister, J., Balmaseda, M. A., Barrett, B., Codron, F., Earnshaw, P., Fast, J., Hannay, C., Kaiser, J. W., Kitagawa, H., Klein, S. A., Köhler, M., Manganello, J., Pan, H.-L., Sun, F., Wang, S., and Wang, Y.: The PreVOCA experiment: modeling the lower troposphere in the Southeast Pacific, Atmos. Chem. Phys., 10, 4757–4774, doi:10.5194/acp-10-4757-2010, 2010. 15944

Zuidema, P., Painemal, D., de Szoeke, S., and Fairall, C.: Stratocumulus cloud-top height estimates and their climatic implications, J. Climate, 22, 4652–4666, 2009. 15927, 15929, 15931

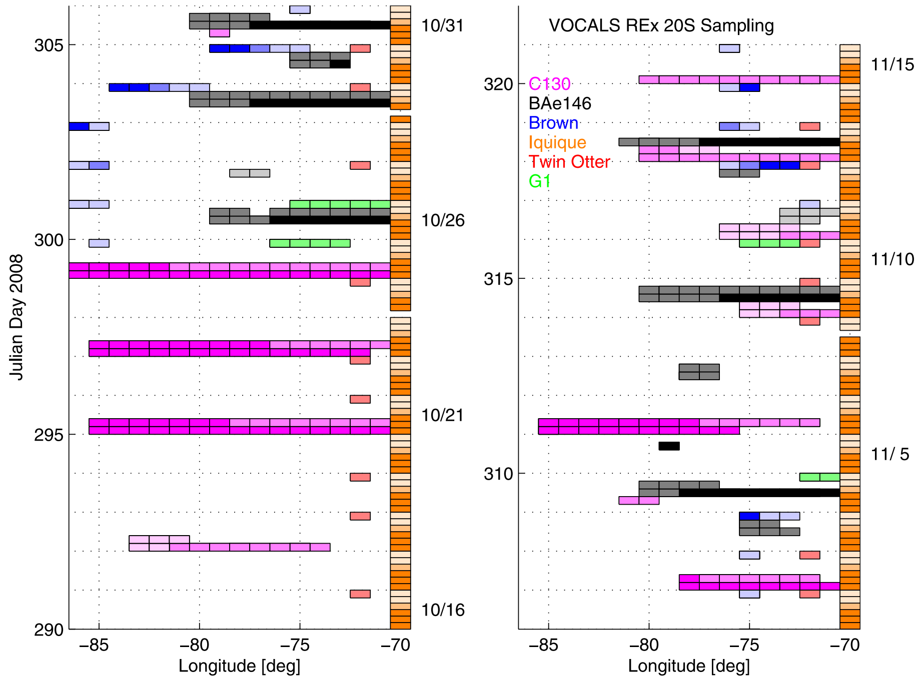

Fig. 1. VOCALS REx sampling within 1° latitude of 20° S. Platforms are color coded and shaded by the measurement time (darkest: 00:00–12:00 UTC (night and dawn), medium: 12:00–16:00 UTC (morning transition), light: 16:00–24:00 UTC (midday and afternoon).

ACPD
10, 15921–15962, 2010

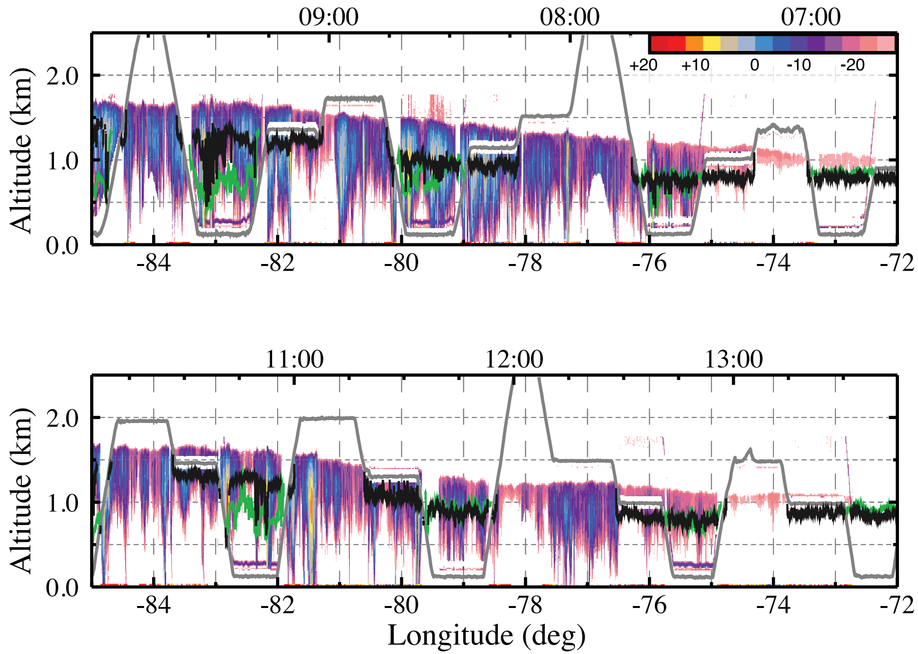

Fig. 2. Longitude-height plot of WCR reflectivity along 20° S for the outbound (top) and return (bottom) portions of C130 RF03. During subcloud legs, the in-situ LCL (green) and the WCL cloud base (black) are superimposed. During cloud legs, the black line shows the cloud base adiabatically derived from in-situ LWC. The grey line traces the aircraft flight track; the top axis labels show UTC time.

ACPD
10, 15921–15962, 2010

VOCALS-REx 20 S boundary layer, clouds and precipitation

C. S. Bretherton et al.

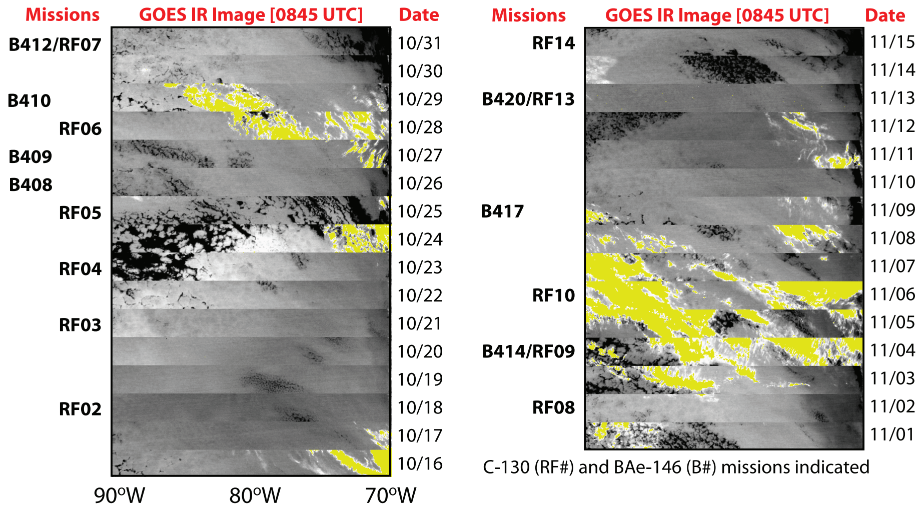

Fig. 3. GOES 12 µm infrared brightness temperature at 08:45 UTC daily from 19–21° S, 70–90° W; C130/BAe146 missions with a substantial 20° S component are indicated at left.

ACPD
10, 15921–15962, 2010

VOCALS-REx 20 S boundary layer, clouds and precipitation

C. S. Bretherton et al.

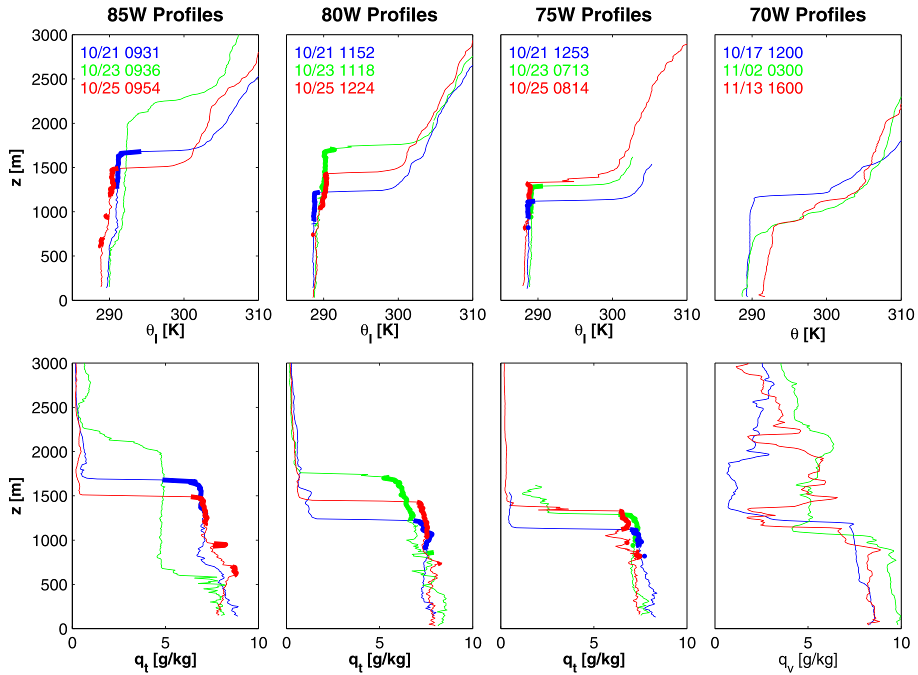

Fig. 4. Representative profiles along 20° S of θ and q_v from Iquique (70° W), and of θ_l and q_t from the C130 near 75, 80 and 85° W. The C130 profiles are thickened where $q_l > 0.02\,\mathrm{g\,kg^{-1}}$.

ACPD
10, 15921–15962, 2010

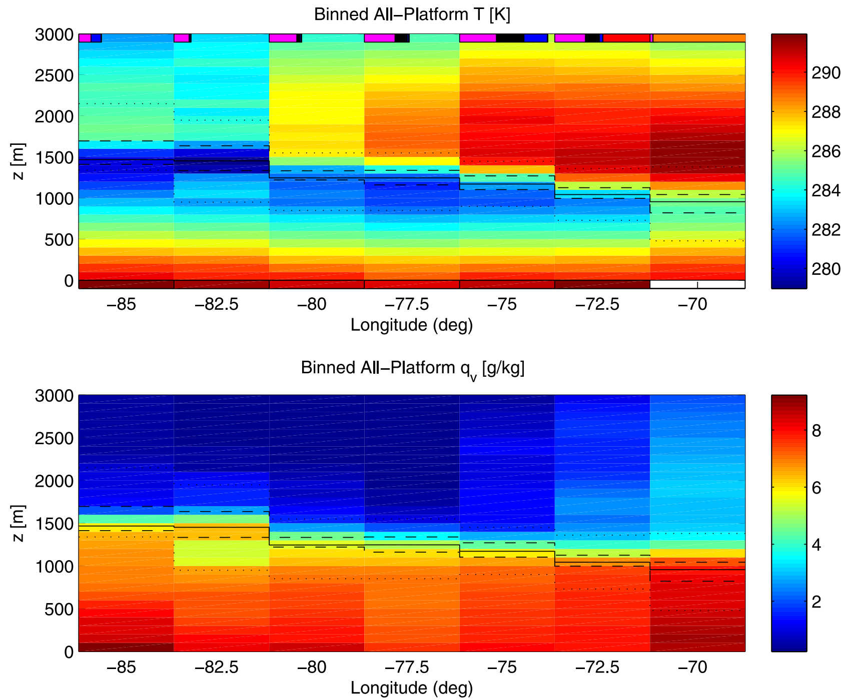

Fig. 5. Multiplatform longitude-height cross-sections of 16 October–15 November 2008 mean T (top) and q_v (bottom) along 20° S in 2.5° longitude and 100 m height bins. In each longitude bin, the statistics of inversion base height (diagnosed as a local temperature minimum) across the contributing profiles are shown using dotted lines for the maximum and minimum, dashed lines for the 25/75 percentiles and a solid line for the median. In the temperature plot, the shades below z=0 show Reynolds SST, and the colored rectangles at the top of each longitude bin indicate the fraction of days in the month with contributing observations from each platform (magenta: C130, black: BAe146 dropsondes, blue: *Brown* sondes, orange: Iquique sondes, red: Twin Otter profiles).

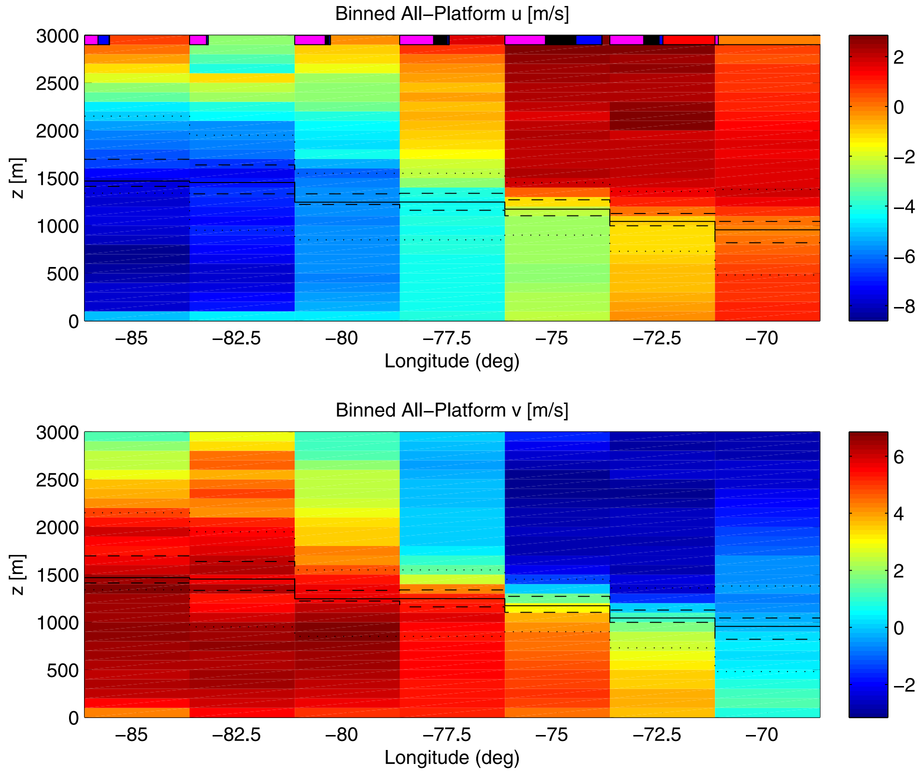

Fig. 6. As in Fig. 5, but for wind components *u* and *v*.

ACPD
10, 15921–15962, 2010

VOCALS-REx 20 S boundary layer, clouds and precipitation

C. S. Bretherton et al.

Title Page
Abstract Introduction
Conclusions References
Tables Figures
◀ ▶
Back Close
Full Screen / Esc
Printer-friendly Version
Interactive Discussion

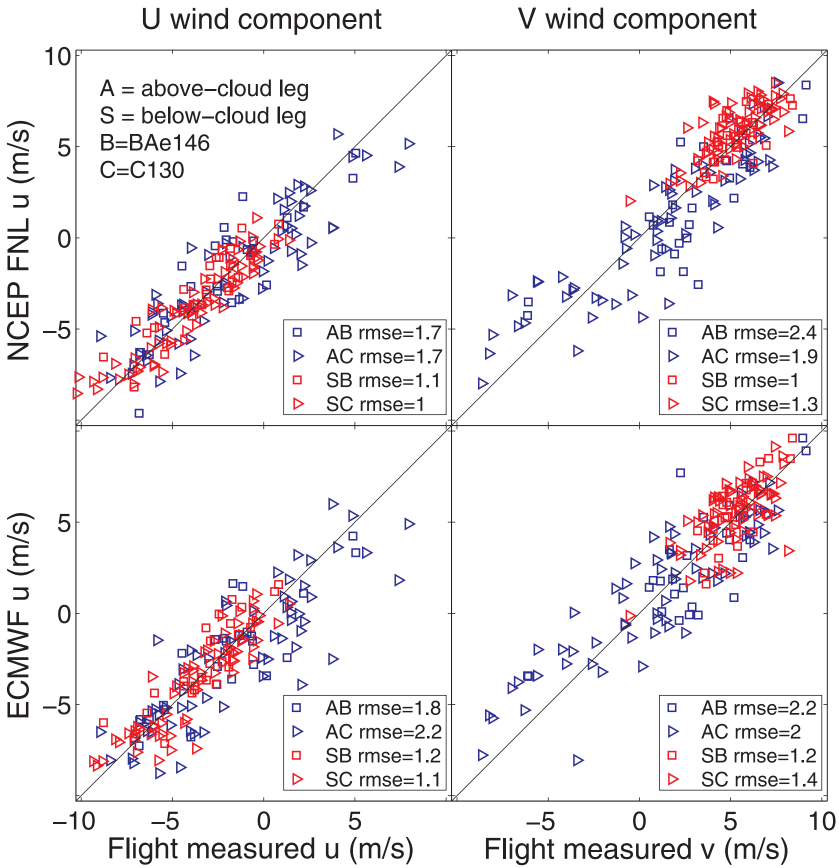

Fig. 7. Scatterplots of observed C130 and BAe146 leg-mean wind components *u* and *v* vs. NCEP FNL (top) and ECMWF operational (bottom) analyses, using all above-cloud (blue) and subcloud (red) legs flown within 1° latitude of 20° S.

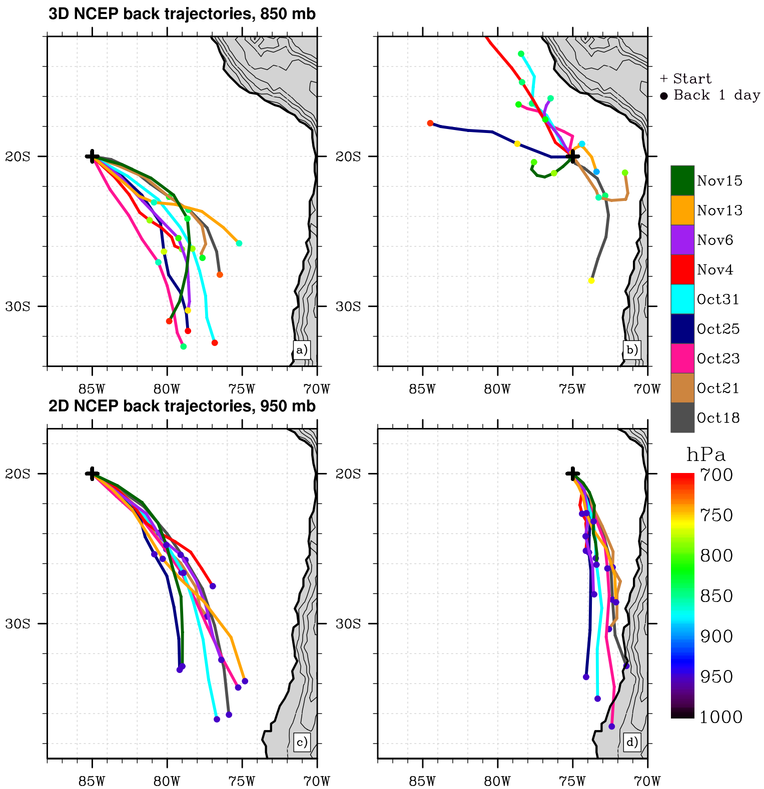

Fig. 8. FNL back-trajectories from 85° W (left) and 75° W (right) for the C130 20° S mission segments, color-coded by flight. Top panels show three-dimensional "free-tropospheric" back-trajectories from 850 hPa (dot shading indicate pressure along the trajectory back one and two days), and bottom panels show horizontal "boundary-layer" back-trajectories using 950 hPa winds. Back-trajectories are initialized at 12:00 UTC for the night flights and 15:00 UTC for the day flights.

ACPD
10, 15921–15962, 2010

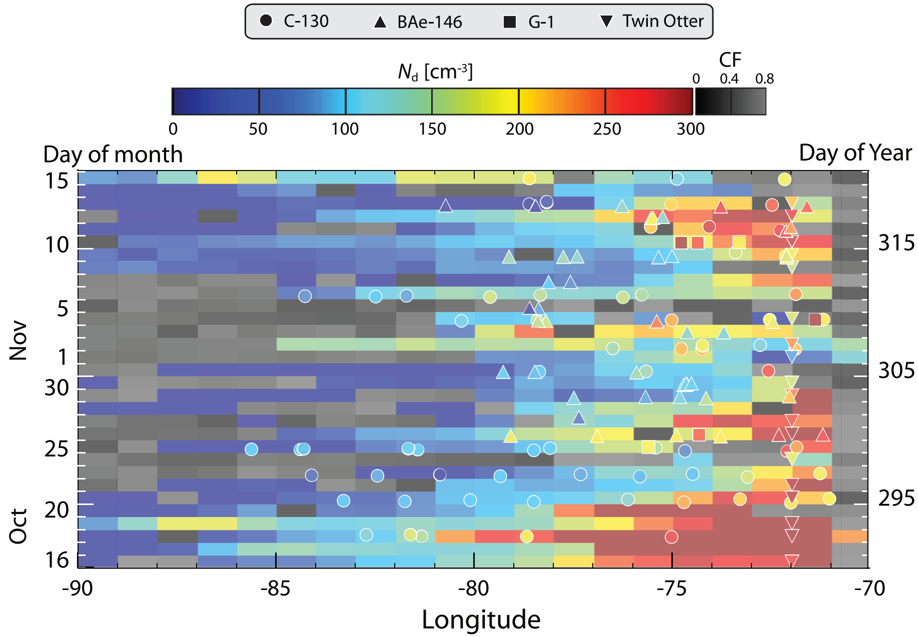

Fig. 9. Comparison of 20° S cloud leg-mean cloud droplet concentration N_d shaded circles (C130) and triangles (BAe146) with daily MODIS-derived cloud droplet concentration along 20° S averaged on a 1°×1° grid (color-shaded rectangles). Grey shades indicate cloud fraction (CF) in regions of broken cloud in which MODIS cannot reliably estimate N_d.

ACPD
10, 15921–15962, 2010

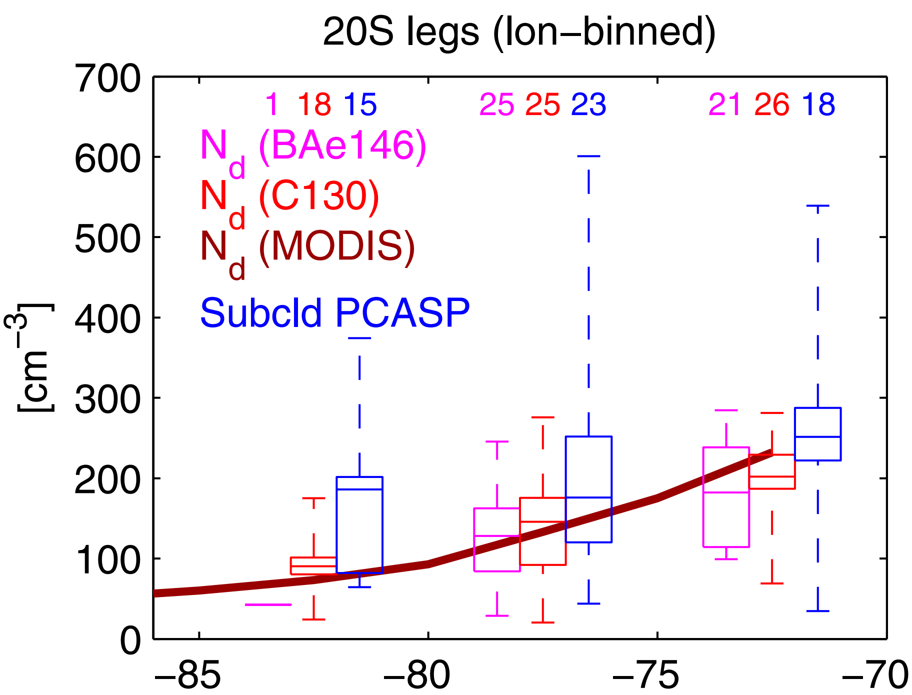

Fig. 10. (left) Boxplots of longitude-binned cloud droplet concentration N_d from 20° S C130 and BAe146 in-cloud legs and PCASP-derived accumulation-mode aerosol concentration from 20° S C130 below-cloud legs. REx-mean MODIS-derived N_d along 20° S from daily satellite overpasses is also shown for comparison. In this and following boxplots, the number of flight legs included in each longitude bin is indicated at the top.

ACPD
10, 15921–15962, 2010

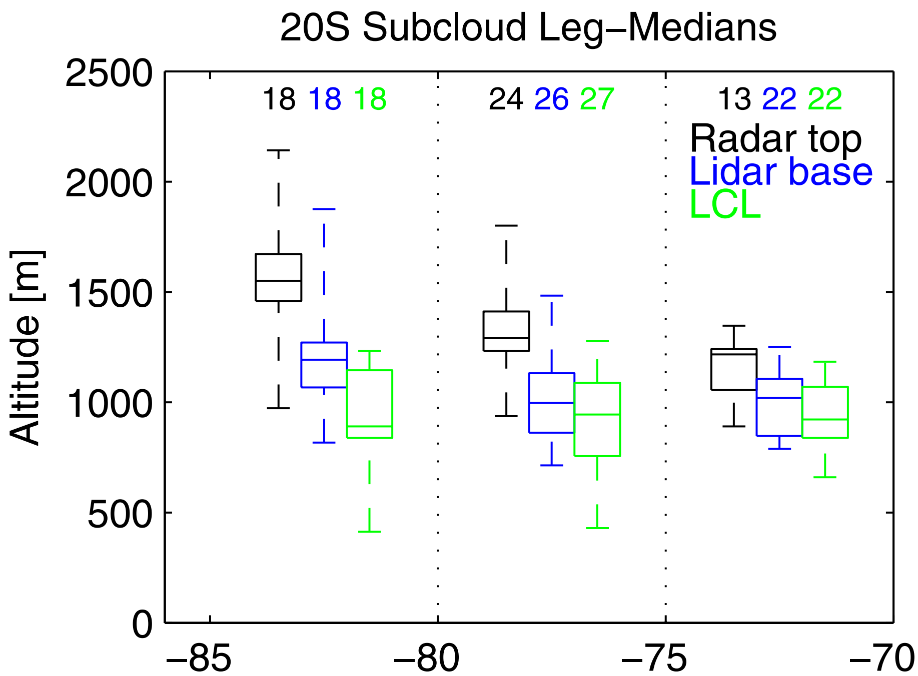

Fig. 11. Boxplots of WCR cloud top, WCL cloud base, and LCL for all 20° S C130 subcloud legs, using a similar format to Fig. 10.

ACPD
10, 15921–15962, 2010

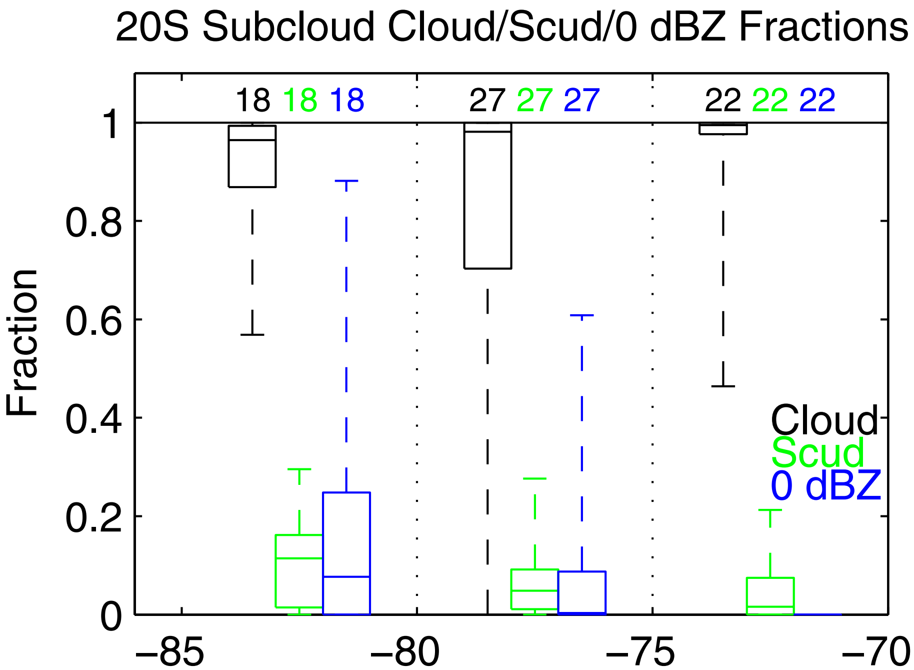

Fig. 12. Boxplots of frequency of cloud, "scud" (cloud with a base more than 100 m below the median), and heavy cloud-base drizzle (WCR column-maximum radar reflectivity > 0 dBZ), from 20° S C130 subcloud legs.

ACPD
10, 15921–15962, 2010

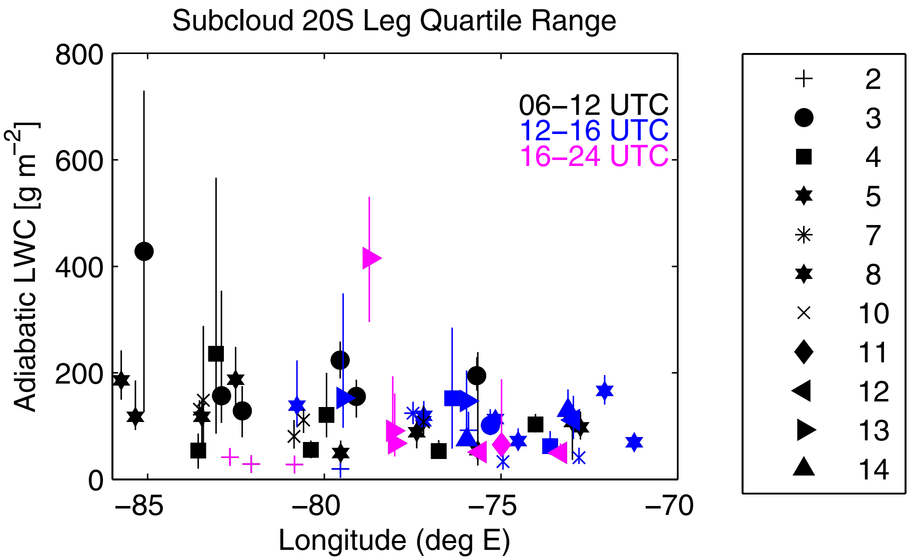

Fig. 13. WCR/WCL-derived adiabatic LWP for 20° S C130 subcloud legs, using flight-specific symbols and color-coded by time of day. Each symbol shows the leg-median LWP, and the vertical lines show the interquartile range of the 1 Hz data for that leg.

ACPD
10, 15921–15962, 2010

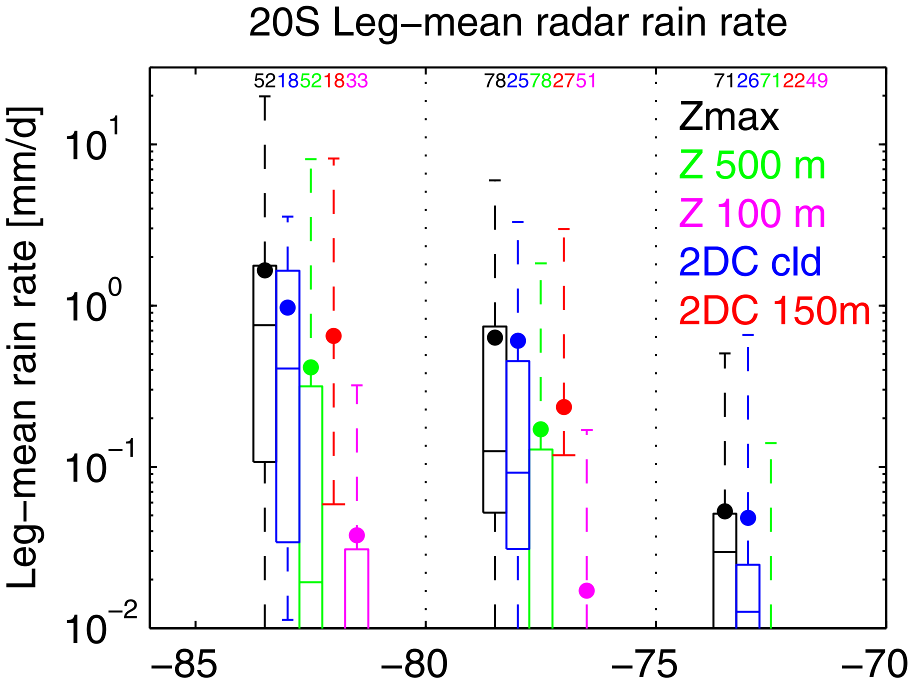

Fig. 14. 20° S leg-mean precipitation rates derived from column-max reflectivity and cloudbase *Z*–*R* (black) , 500 m reflectivity and cloud base *Z*–*R* (green), 100 m reflectivity and surface *Z*–*R* (pink), 2D-C raindrop size distribution from in-cloud legs (blue) and subcloud legs (red). Colored dots show the mean over all legs in each longitude bin.

ACPD
10, 15921–15962, 2010

Title Page
Abstract
Introduction
Conclusions
References
Tables
Figures
◀◀
▶▶
◀
▶
Back
Close
Full Screen / Esc
Printer-friendly Version
Interactive Discussion

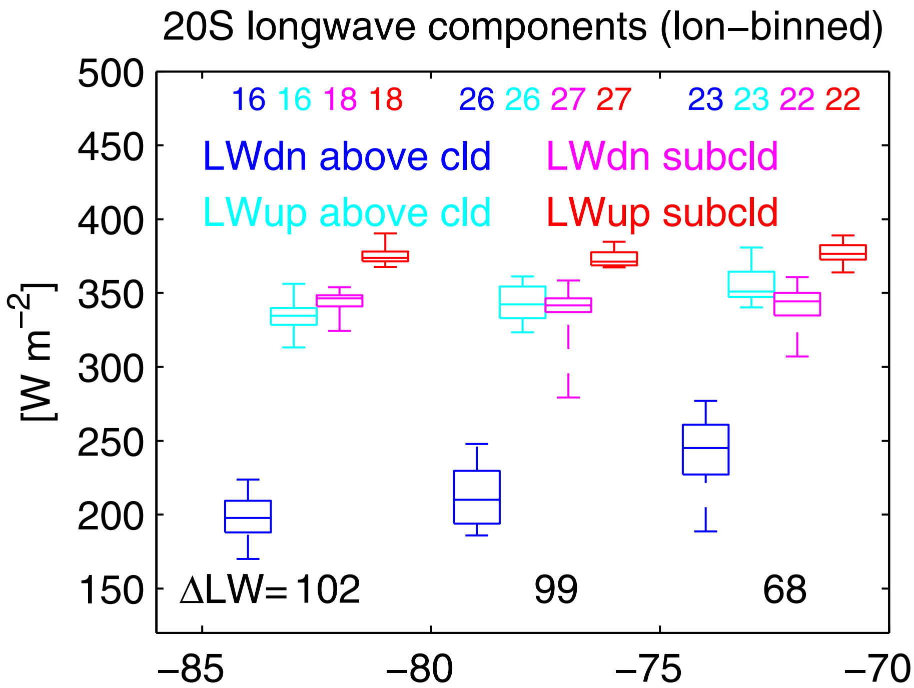

Fig. 15. Longitude-binned C130 broadband longwave radiative flux components from above-cloud and below-cloud 20° S legs. Bottom: Inferred mean longwave radiative flux divergence across the boundary layer, ΔLW [W m^{-2}], for each longitude bin.

ACPD
10, 15921–15962, 2010

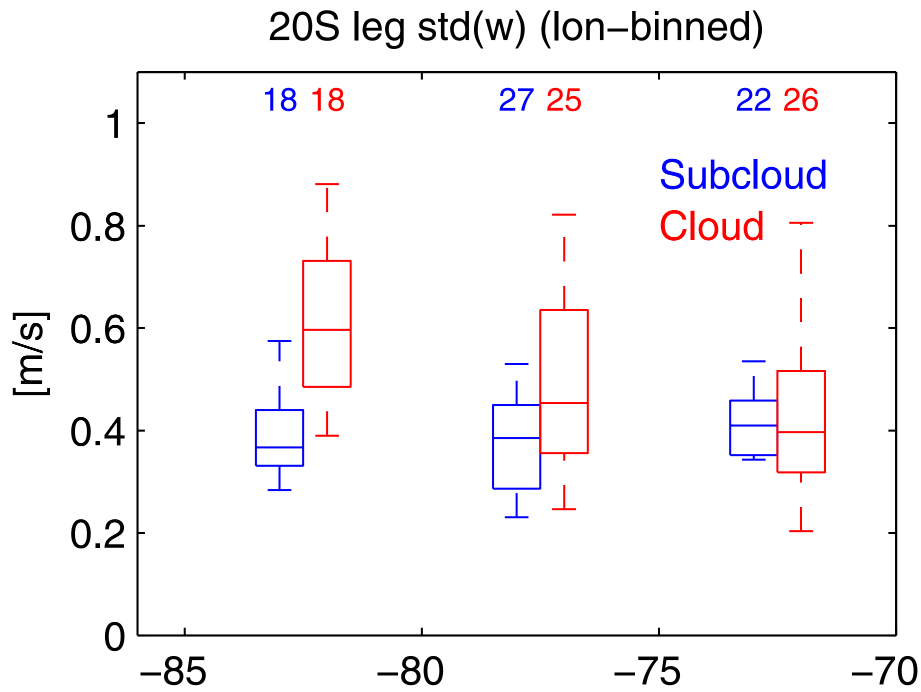

Fig. 16. Standard deviation of *w* from C130 20° S legs: **(a)** in-cloud, **(b)** subcloud.